Sub-Terahertz Spatial Statistical MIMO Channel Model for Urban Microcells at 142 GHz

Shihao Ju and Theodore S. Rappaport

NYU WIRELESS, Tandon School of Engineering, New York University, Brooklyn, NY, 11201

{shao, tsr}@nyu.edu

Abstract—**Sixth generation (6G) cellular systems are expected to extend the operational range to sub-Terahertz (THz) frequencies between 100 and 300 GHz due to the broad unexploited spectrum therein. A proper channel model is needed to accurately describe spatial and temporal channel characteristics and faithfully create channel impulse responses at sub-THz frequencies. This paper studies the channel spatial statistics such as the number of spatial clusters and cluster power distribution based on recent radio propagation measurements conducted at 142 GHz in an urban microcell (UMi) scenario. For the 28 measured locations, we observe one to four spatial clusters at most locations. A detailed spatial statistical multiple input multiple output (MIMO) channel generation procedure is introduced based on the derived empirical channel statistics. We find that beamforming provides better spectral efficiency than spatial multiplexing in the LOS scenario due to the boresight path, and two spatial streams usually offer the highest spectral efficiency at most NLOS locations due to the limited number of spatial clusters.**

Index Terms—**Channel Measurement; Channel Modeling; Spatial Statistics; Beamforming; Spatial Multiplexing; MIMO; Sub-Terahertz; 140 GHz; 5G; 6G**

I. Introduction

As millimeter-wave wireless systems have been gradually deployed for the fifth-generation (5G) communications, Terahertz (THz) frequencies are expected to play an essential part in the sixth-generation (6G) and beyond, which can provide a tenfold increase in bandwidth [1]. Sub-THz frequencies (100 GHz - 300 GHz) have been considered the next frontier leading to THz communications over the past few years [2]. Some early works on channel measurements and modeling at 140 GHz have been presented in the literature [3]–[6]. In addition, recent advances in phased arrays, complementary metal–oxide–semiconductor (CMOS)-based power amplifiers, and low noise amplifiers at sub-THz frequencies [7]–[9] show that sub-THz wireless systems may become a reality in the near future.

As the carrier frequency increases, the free space path loss increases quadratically according to the Friis' law under the assumption of constant antenna gains [10]. However, the decreasing wavelength at sub-THz frequencies enables tightly packing a larger number of antenna elements into a small form factor. If the physical size of the antenna array (effective aperture) is kept constant at both transmitter (TX) and receiver

(RX), theoretically, a quadratic decrease in the free space path loss is expected with increasing frequencies [11].

Antenna arrays with many antenna elements also bring challenges in many aspects such as signal processing and array modeling [12]–[15]. On the one hand, tightly packed arrays lead to high correlation and mutual coupling across antenna elements [16]. On the other hand, fully digital processing adopted in conventional multiple input multiple output (MIMO) systems at sub-6 GHz may not be realistic for large arrays at sub-THz frequencies since one radio frequency (RF) chain per antenna element will cause prohibitively high power consumption, hardware complexity, and cost [13]. Thus, hybrid beamforming was proposed by combining the baseband digital processing with the RF analog processing using phase shifters [14], [15], [17]. Even though phase shifters induce constant modulus constraints (i.e., the amplitude of signals cannot be changed) [14], the low cost and near-optimal performance make hybrid beamforming a promising solution for the 5G and beyond [15]. Such hybrid architecture employs a few RF chains at the baseband precoding stage and a large number of phase shifters (one or two orders of quantity more than the number of RF chains) to realize spatial multiplexing and beamforming simultaneously.

This paper aims to understand the spatial channel statistics and to evaluate the spectral efficiency of beamforming and spatial multiplexing schemes of sub-THz signals. First, we present the propagation channel measurements conducted at 142 GHz in an urban microcell (UMi) scenario in Section II. The statistics of channel spatial parameters such as the number of spatial clusters, cluster power, and omnidirectional root mean square (RMS) angular spread are derived in Section III. Section IV gives a bi-directional MIMO channel generation procedure. Section V statistically generates channel impulse responses by implementing the above channel generation procedure and analyzes the spectral efficiency transmitting different number of data streams for a single user. Finally, concluding remarks are provided in Section VI.

II. 142 GHz UMi Channel Measurements

The 142 GHz UMi channel measurements were conducted in the fall of 2020 on the NYU engineering campus in Downtown Brooklyn, NY, to gain knowledge of potential performance of beamforming and spatial multiplexing of sub-THz wireless systems. As shown in Fig. 1, the engineering

campus includes a square with a size of ~100 m by 100 m, which is surrounded by tall concrete buildings and narrow street canyons, representing a regular UMi scenario. There are glass widows, trees, pedestrians, metal lampposts, and concrete pillars in the surrounding environment causing reflections and scattering.
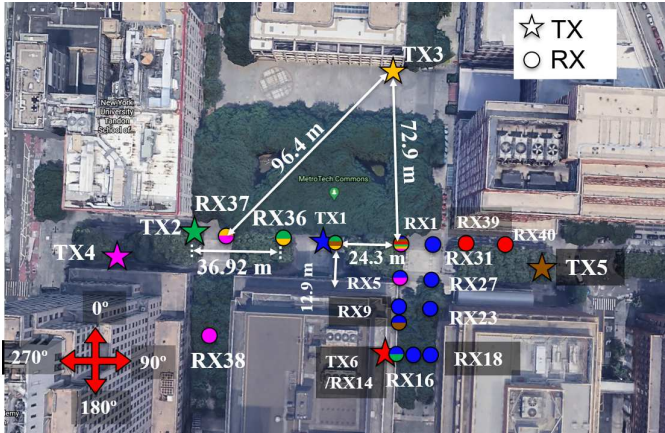

Fig. 1: 142 GHz outdoor UMi measurement locations [18]. TX locations are denoted as stars in different colors. RX locations are denoted as circles. One RX location filled with multiple colors indicates that the channels between this RX location and multiple TX locations were measured.

A wide range of TX and RX locations were selected for various propagation distances and environments (line-of-sight [LOS] and non-LOS [NLOS]) in order to emulate small cells for sub-THz wireless systems. The TX was deployed at a height of 4 m above ground level serving as a small cell base station (BS), and the RX was placed at a height of 1.5 m above ground level serving as a mobile user (UE). The TX and RX location pairs are provided in Table I. Overall, there are 16 LOS location pairs and 12 NLOS location pairs with TX-RX (T-R) separation distances from 12.9 m to 117.4 m.

Highly directional horn antennas with 27 dBi gain and 8° half-power beamwidth (HPBW) were used at both TX and RX to compensate for the large free space path loss within the first-meter propagation at 142 GHz. The horn antennas and the up/down-converter modules were mounted on electrically controllable gimbals, rotating in the azimuth and elevation planes with a sub-degree resolution. A 500 MHz 11th order pseudorandom m-sequence was generated at the TX baseband and mixed with an intermediate frequency of 7 GHz, then up-converted to a center frequency of 142 GHz. A sliding correlation based receiver was used at the RX, which can provide 39 dB processing gain. The null-to-null RF bandwidth is 1 GHz, which corresponds to a temporal resolution of 2 ns for multipath components (MPCs) [11]. The maximum measurable path loss was 152 dB with a minimum signal-to-noise (SNR) requirement of 5 dB. At each TX and RX location pair, the best TX and RX pointing angles in which the RX received the strongest power were first found and set as the starting points of TX and RX, respectively. The LOS measurements have the TX and RX antennas on boresight, and the

TABLE I: MEASURED TX AND RX LOCATION PAIRS

TX	LOS RX	NLOS RX
TX1	RX1, RX5, RX23, RX27, RX31	RX9, RX14, RX16, RX18
TX2	RX1, RX35, RX36	RX14
TX3	RX35, RX36, RX37	RX1
TX4	RX3, RX37	RX1, RX38
TX5	RX3, RX35	RX1, RX10
TX6	RX1	RX39, RX40

NLOS measurements have the TX and RX antennas pointing to the strongest receiving direction by manually searching over azimuth and elevation planes. Then, we fixed the TX pointing angle and swept the RX in the azimuth plane in a step size of the antenna HPBW (8°). Each azimuth sweep performed 45 stepped-rotations (360/8=45) and measured 45 directional PDPs. We then performed two identical azimuth sweeps in different elevation planes by uptilting and downtilting the RX by 8°. Overall, three RX sweeps produced 135 directional PDPs for one TX pointing angle. The TX was then pointed to some manually selected directions in which the RX detected signal energy above the noise floor. The identical three RX azimuthal sweeps were performed for each individual TX pointing angle. Most TX and RX location pairs have one to three distinct angles of departure (AOD) and angles of arrival (AOA). A sample measured directional PDP having three MPCs is shown in Fig. 2. Note that most measured directional PDPs have only one MPC due to the narrow beamwidths of the TX and RX antennas.
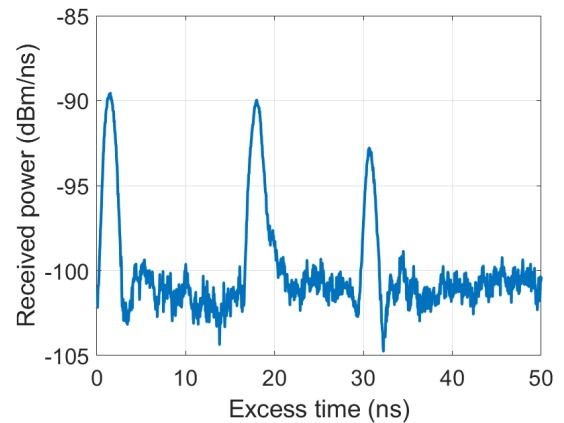

Fig. 2: The directional excess time PDP was measured at TX1 and RX14. The received power was recovered by removing system processing gain and antenna gain.

III. CHANNEL SPATIAL STATISTICS AT 142 GHz

Measurements with narrowbeam horn antennas provide a convenient way to understand channel spatial statistics for sub-THz frequencies. The angular resolution of measurements is limited by the antenna HPBW (8° in this measurements). Even though the azimuth sweeps were performed at three elevation angles, we did not observe two distinct MPCs arriving in a

(a) LOS AOA APS: TX1 and RX5

(b) LOS AOA APS: TX3 and RX35

(c) NLOS AOA APS: TX5 and RX1
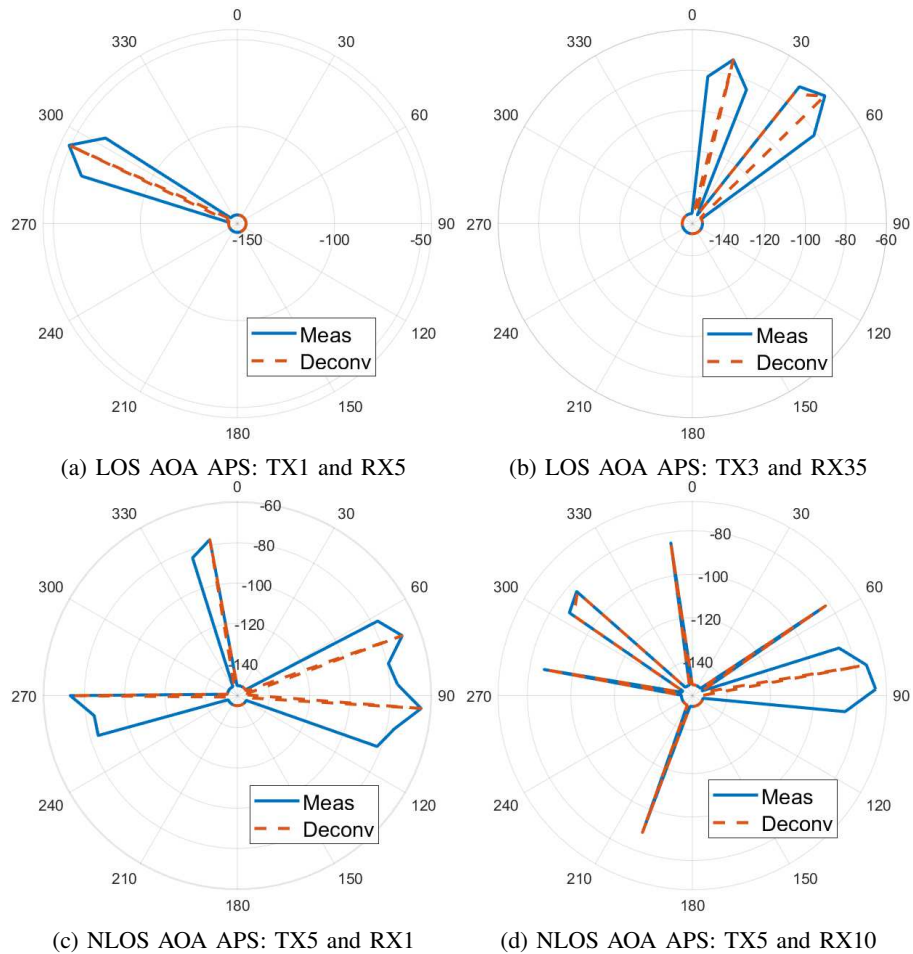
(d) NLOS AOA APS: TX5 and RX10

Fig. 3: 2-D AOA angular power spectrum plots with different number of spatial clusters in the boresight elevation angle with a threshold of 20 dB in the directional received power.

similar azimuth angle but different elevation angles. Thus, we extracted spatial statistics only using the directional measurements conducted in the boresight elevation plane.

Four sample AOA angular power spectrums are shown in Fig. 3. The threshold of the angular power spectrum is set to be 20 dB down from the strongest directional power in the azimuth plane. Fig. 3a shows the angular power spectrum of a LOS location pair (TX1 and RX5), which only has the boresight path. Fig. 3b shows the angular power spectrum of another LOS location pair (TX3 and RX35), which has not only the boresight path but a reflected path from a metal lamppost. From Fig. 3a and Fig. 3b, we can see that the two neighboring directions next to the peak direction have an approximately 12 dB drop in the received power, which can be the side effect of the horn antenna pattern, which motivates us to recover the actual direction of the arriving signals by deconvolving the antenna pattern out of the angular power spectrum. Thus, the radiation pattern of the employed antennas were measured, and the deconvolved angular power spectrum of AOA are also shown in Fig. 3 as dashed lines.

Fig. 3c plots the angular power spectrum of an NLOS location pair (TX5 and RX1) showing three spatial lobes. A spatial

lobe is defined as a main direction of arrival or departure where multipath components can arrive over hundreds of nanoseconds [2], [19]. The spatial lobes are extracted by partitioning the angular power spectrum with a spatial lobe threshold (e.g., 20 dB used in this paper). A set of consecutively measured directions having powers above the spatial lobe threshold forms a spatial lobe. Fig. 3d plots the angular power spectrum of another NLOS location pair (TX5 and RX10) showing six spatial lobes, which is the maximum number of spatial lobes we observed during measurements. Note that in Fig. 3c, the angular power spectrum has a wide spatial lobe centered at 90° with two peaks, indicating that two signals were received relatively close in space (∼24° apart) forming a single spatial lobe. Such two signals can be recovered by a deconvolution of the antenna pattern or through peak searching. Due to the limitation of the angular resolution, the subpaths within each signal cannot be resolved in space. We call such a signal a spatial cluster in the rest of this paper. Compared to the definition of spatial lobes, the number of spatial clusters should be no less than the number of spatial lobes. The statistics of spatial clusters will be shown as follows and used in the MIMO channel generation in Section IV.

A. The number of spatial clusters

The number of spatial clusters (N_c) is inversely proportional to the selected threshold. The histogram of the number of measured spatial clusters over all 28 LOS and NLOS locations in the 142 GHz UMi scenario and the fit Poisson distribution with a mean of 1.15 are shown in Fig. 4. Since the Poisson starts from zero, and only measurement locations with no outage are considered (i.e., at least one spatial cluster), $N'_c = N_c - 1$ is used in the distribution fitting. The Poisson distribution is given by

$$\Pr(N'_c = k) = \lambda_c^k \exp(-\lambda_c)/k!, \tag{1}$$

where λ_c is the mean of N'_c. k can be any integer between zero and five since the maximum number of observed spatial clusters is six. λ_c is 0.69 and 1.82 for the separate LOS and NLOS locations, respectively, showing that NLOS locations have more directions of arrival.
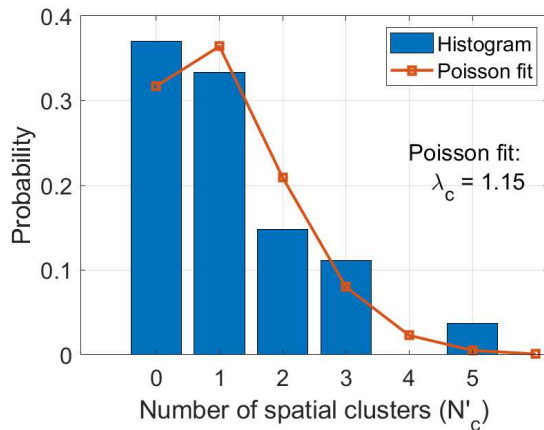

Fig. 4: The number of spatial clusters for 142 GHz UMi is well fitted by a Poisson distribution (1) with $\lambda_c = 1.15$.

B. Spatial cluster powers

The received power within each spatial cluster indicates the path quality and determines the practical performance of beamforming and spatial multiplexing implementations. Thus, the distribution of received powers is a key channel indicator for multiple data stream transmission. The normalized cluster powers at each location are calculated by $\bar{P}_i = P_i / \sum_{j=1}^{N_c} P_j$. P_i is the received power in the ith cluster, and $\bar{P}_i$ is the normalized cluster power. The order of spatial clusters is determined based on the received power. The first spatial cluster bears the strongest received power. The power distribution among clusters can be modeled as an exponential decaying function of the order of clusters [2]:

$$P_i = ae^{-i/b}10^{c_i/10}, \tag{2}$$

where $ae^{-i/b}$ represents the average power within the ith cluster, and c_i is a shadowing term modeled as a normal random variable with zero mean and a standard deviation of σ_c in dB scale. The cluster power distribution at all LOS and NLOS locations and the fit decaying exponential function with $a = 0.88$ and $b = 0.57$ are shown in Fig. 5. a are 0.96 and 0.76,

and b are 0.03 and 0.81 for separate LOS and NLOS scenarios, respectively, showing the single LOS cluster occupies almost all the received power in the LOS scenario whereas the NLOS locations have more clusters bearing comparable powers.
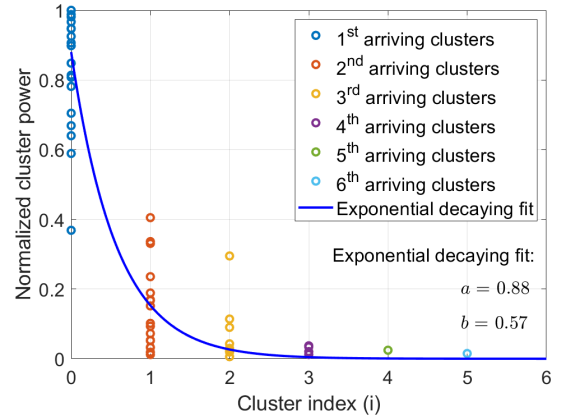

Fig. 5: Normalized cluster powers for 142 GHz UMi are well modeled by an exponential decaying function (2) with $a = 0.88$ and $b = 0.57$.

C. Omnidirectional RMS angular spread

Omnidirectional RMS angular spread is an important indicator of angular dispersion of MPCs. Large omnidirectional RMS angular spread suggests that spatial clusters are well separated in the space, which may be beneficial for spatial multiplexing. The empirical cumulative probability function (CDF) of omnidirectional RMS angular spread is shown in Fig. 6, where the maximum, mean, and median values are 65.33°, 16.66°, and 8.84°. 0°RMS angular spread suggests that only one spatial cluster exists in the space.
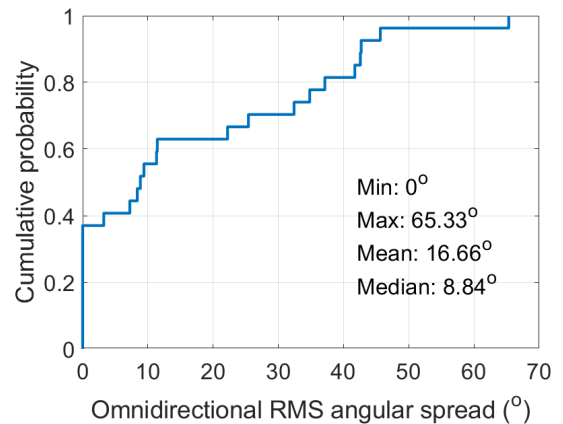

Fig. 6: CDF of omnidirectional RMS angular spread.

IV. SUB-THZ MIMO CHANNEL GENERATION PROCEDURE

A double directional MIMO channel generation procedure is presented step by step using the spatial statistics derived in Section III. Due to the lack of relative timing information of signals measured in different directions, a narrowband spatial channel model is assumed here, and a corresponding wideband channel model will be presented in future work.

1) Step 1: Generate the large-scale path loss using the 1 m close-in (CI) free space reference distance path loss model [2], [3], [20]:

$$\text{PL}^{\text{CI}}(f, d)[\text{dB}] = \text{FSPL}(f, 1\,\text{m}) + 10n \log_{10}(d) + \chi_\sigma, \quad (3)$$

where $\text{FSPL}(f, 1\,\text{m}) = 20 \log_{10}(4\pi f/c)$. n is path loss exponent (PLE) and d is the 3-D T-R separation distance in meters. Shadow fading χ_σ is modeled by a zero mean Gaussian random variable with standard deviation σ in dB. The n and σ for 142 GHz outdoor UMi scenario is given in [18], which are 1.94 and 2.66 for the LOS locations, and 2.87 and 8.22 for the NLOS locations. The simulated TX-RX separation distance ranges from 10 to 100 m to agree with the measurements.

2) Step 2: Generate the number of spatial clusters using (1). Note that the maximum number of generated spatial clusters is limited to six.

3) Step 3: Generate the azimuth AOA and AOD of each spatial cluster. The azimuth plane is equally divided into as many sectors as the number of generated spatial clusters. The central angle of each spatial cluster is uniformly selected in the assigned sector.

4) Step 4: Generate the cluster powers using (2). Note that the generated cluster powers are randomly coupled with the generated cluster angles.

5) Step 5: Generate the phase of each cluster. Because the absolute propagation time of each spatial cluster is unknown, it is reasonable to generate phases following a uniform distribution between 0 and 2π.

6) Step 6: Generate the MIMO channel matrix according to the array geometry:

$$\mathbf{H} = \sum_{i=1}^{N_c} \alpha_i e^{j\psi_i} \mathbf{a}_r(\phi_i^r, \theta_i^r) \mathbf{a}_t(\phi_i^t, \theta_i^t)^H \quad (4)$$

where α_i and ψ_i denote the channel gain and phase of the ith cluster, respectively. N_t and N_r are the number of antenna elements at the TX and RX. ϕ_i^r and θ_i^r are the AOA and ZOA in the global coordinate system (GCS). ϕ_i^t and θ_i^t are the AOD and ZOD in the GCS. $\mathbf{a}_t$ and $\mathbf{a}_r$ are the spatial signatures of TX and RX antenna arrays, respectively. The superscript H represents the complex conjugate transpose. In this paper, uniform rectangular arrays (URAs) placed in the y-z plane are used at both TX and RX. Such a URA with a size of N elements has N_h elements along the y-axis and N_v elements along the z-axis. The spatial signature is given by [15]

$$\mathbf{a}(\phi_i, \theta_i) = \frac{1}{\sqrt{N}}[1, ..., e^{j2\pi \frac{d}{\lambda}(p\sin(\phi_i)\sin(\theta_i) + q\cos(\theta_i))},$$
$$..., e^{j2\pi \frac{d}{\lambda}((N_h-1)\sin(\phi_i)\sin(\theta_i) + (N_v-1)\cos(\theta_i))}]^T, \quad (5)$$

where d and λ are the antenna space and the signal wavelength. $0 \le p \le N_h - 1$ and $0 \le q \le N_v - 1$ are the indices of antenna elements in the 2-D plane.

V. SPECTRAL EFFICIENCY ANALYSIS

Here, we consider a single-cell downlink transmission. Transmit beamforming (precoding) can direct the beam into the direction of the strongest signal using the information
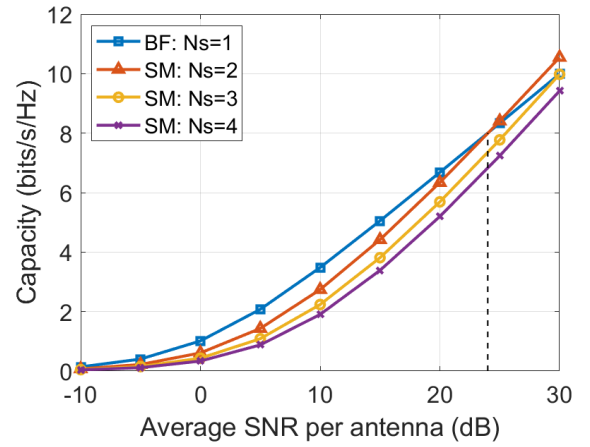
(a) Spectral efficiency in the LOS scenario.
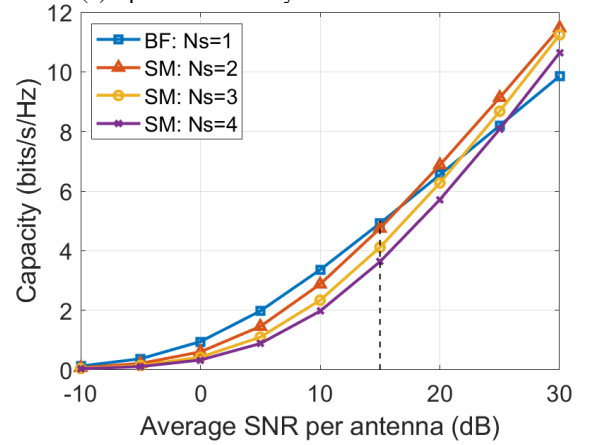
(b) Spectral efficiency in the NLOS scenario.

Fig. 7: Spectral efficiency for different number of streams in LOS and NLOS scenarios.

of channel matrix obtained via either channel reciprocity or feedback [21]. Spatial multiplexing enables the TX to transmit different data streams through different MPCs to increase spectral efficiency. Beamforming can be considered a special case of spatial multiplexing with one data stream. Ideally, spatial multiplexing should always have a higher spectral efficiency than beamforming due to the additional spatial degree of freedom [22]. However, several practical constraints make spatial multiplexing unfavorable such as MPC richness and transmit power. Sparse channels at mmWave and sub-THz frequencies in the outdoor environment may not have enough spatial degree of freedom to support high-order spatial multiplexing [19]. Thus, transmit power needs to be concentrated into only a few strongest directions rather than being split into many beams when the average SNR is low.

To evaluate the impact of two transmission schemes on the MIMO system throughput, we create thousands of sample channels following the procedure described in Section IV. The UEs are randomly dropped in the distance range between 10 and 100 m. A 16×8 URA and a 4×2 URA are deployed at the BS and UE, respectively. Each antenna element is a patch antenna with a length of one wavelength (e.g., 2.11 mm at 142 GHz) and a width of half wavelength, having a

maximum directivity of 10.4 dBi and 56° HPBW. The antenna plane is initially set in the y-z plane, and then the broadside is rotated to the direction of the strongest cluster. The number of data streams is set from one to four to investigate the spatial multiplexing gain. The total transmit power is 0 dBm and constant for different number of streams.

We assume that the channel state information is known at the BS, which forms a closed-loop spatial multiplexing. The transmit precoding vector and the receive combining vector are chosen based on the right and left singular vectors of the channel $\mathbf{H}$ via the SVD decomposition based on the eigen beamforming (EBF) approach. Fig. 7 shows the spectral efficiencies for different numbers of data streams in the LOS and NLOS scenarios. It should be noted that the beamforming scheme outperforms the spatial multiplexing schemes in the low-SNR region. Spatial multiplexing starts providing additional benefits above a certain SNR threshold, which are 24 dB and 15 dB for the LOS and NLOS scenarios, respectively, suggesting that the LOS path is stronger than the other reflected paths (e.g., 5-15 dB), and the transmit power should be mainly allocated in the LOS direction unless the average SNR in the channel is higher than the threshold. Beamforming should be preferred due to the significant beamforming gain provided by the antenna arrays with massive elements. However, the spatial multiplexing may be much more beneficial in the NLOS environment once the SNR is over 15 dB since the received powers within different spatial clusters are more comparable. In this UMi measurement dataset, we observe two streams can provide higher spectral efficiency than three or four streams at most measured NLOS locations. Even though the maximum number of measured spatial clusters is six, those weak clusters cannot be used for reliable transmission. The cluster power distribution in Fig. 5 also indicates that the late-arriving clusters bear much less power than the first few arriving clusters.

VI. Conclusion

This paper presents a spatial statistical MIMO channel model for sub-THz frequencies in the outdoor UMi scenario. 28 TX and RX locations over a wide range of distance from 12.9 m to 117.4 m were selected in an urban open square to conduct propagation measurements at 142 GHz. The number of spatial clusters was modeled as a Poisson random variable, and the average number of spatial clusters is about two over all measurement locations. Thousands of sample channel matrices were simulated using the proposed statistical channel model and used to predict spectral efficiency using either beamforming or spatial multiplexing. Results showed that beamforming may provide higher spectral efficiency when a dominant LOS path exists in the environment. Spatial multiplexing is preferred at most NLOS locations since multiple reflection paths contain comparable signal energy.

References

[1] T. S. Rappaport *et al.*, "Wireless communications and applications above 100 GHz: Opportunities and challenges for 6G and beyond," *IEEE Access*, vol. 7, pp. 78 729–78 757, June 2019.

[2] S. Ju, Y. Xing, O. Kanhere, and T. S. Rappaport, "Millimeter wave and sub-terahertz spatial statistical channel model for an indoor office building," *IEEE Journal on Selected Areas in Communications*, vol. 39, no. 6, pp. 1561–1575, 2021.

[3] Y. Xing, T. S. Rappaport, and A. Ghosh, "Millimeter wave and sub-thz indoor radio propagation channel measurements, models, and comparisons in an office environment," *IEEE Comm. Letters*, pp. 1–1, 2021.

[4] Y. Chen, Y. Li, C. Han, Z. Yu, and G. Wang, "Channel measurement and ray-tracing-statistical hybrid modeling for low-terahertz indoor communications," *IEEE Transactions on Wireless Communications*, June 2021.

[5] W. Xia, V. Semkin, M. Mezzavilla, G. Loianno, and S. Rangan, "Multi-array designs for mmwave and sub-THz communication to UAVs," in *2020 IEEE 21st International Workshop on Signal Processing Advances in Wireless Communications (SPAWC)*. IEEE, 2020, pp. 1–5.

[6] N. A. Abbasi, A. F. Molisch, and J. C. Zhang, "Measurement of directionally resolved radar cross section of human body for 140 and 220 GHz bands," in *2020 IEEE Wireless Communications and Networking Conference Workshops (WCNCW)*, 2020, pp. 1–4.

[7] D. Yamazaki, Y. Otsuki, T. Hara, N. N. M. Khanh, and T. Iizuka, "11 Gb/s 140 GHz OOK modulator with 24.6 dB isolation utilising cascaded switch and amplifier-based stages in 65 nm bulk CMOS," *IET Circuits, Devices & Systems*, vol. 14, no. 3, pp. 322–326, 2020.

[8] R. Xu *et al.*, "140 GHz additive manufacturing low-cost and high-gain fabry-perot resonator antenna," in *2020 International Workshop on Antenna Technology (iWAT)*. IEEE, 2020, pp. 1–4.

[9] A. Hamani, A. Siligaris, B. Blampey, C. Dehos, and J. L. G. Jimenez, "A 125.5-157 GHz 8 dB NF and 16 dB of gain D-band low noise amplifier in CMOS SOI 45 nm," in *2020 IEEE/MTT-S International Microwave Symposium (IMS)*. IEEE, 2020, pp. 197–200.

[10] T. S. Rappaport, *Wireless Communications: Principles and Practice*, 2nd ed. Upper Saddle River, NJ: Prentice Hall, 2002.

[11] Y. Xing and T. S. Rappaport, "Propagation measurement system and approach at 140 GHz-moving to 6G and above 100 GHz," in *2018 IEEE Global Communications Conference (GLOBECOM)*, 2018, pp. 1–6.

[12] L. Lu, G. Y. Li, A. L. Swindlehurst, A. Ashikhmin, and R. Zhang, "An overview of massive mimo: Benefits and challenges," *IEEE Journal of Selected Topics in Signal Processing*, vol. 8, no. 5, pp. 742–758, 2014.

[13] O. E. Ayach, S. Rajagopal, S. Abu-Surra, Z. Pi, and R. W. Heath, "Spatially sparse precoding in millimeter wave MIMO systems," *IEEE Transactions on Wireless Communications*, vol. 13, no. 3, pp. 1499–1513, 2014.

[14] S. Sun, T. S. Rappaport, M. Shafi, and H. Tataria, "Analytical framework of hybrid beamforming in multi-cell millimeter-wave systems," *IEEE Transactions on Wireless Communications*, vol. 17, no. 11, pp. 7528–7543, Nov 2018.

[15] X. Yu, J.-C. Shen, J. Zhang, and K. B. Letaief, "Alternating minimization algorithms for hybrid precoding in millimeter wave MIMO systems," *IEEE Journal of Selected Topics in Signal Processing*, vol. 10, no. 3, pp. 485–500, 2016.

[16] Y. Gao, R. Ma, Y. Wang, Q. Zhang, and C. Parini, "Stacked patch antenna with dual-polarization and low mutual coupling for massive MIMO," *IEEE Transactions on Antennas and Propagation*, vol. 64, no. 10, pp. 4544–4549, 2016.

[17] N. Song, H. Sun, and T. Yang, "Coordinated hybrid beamforming for millimeter wave multi-user massive MIMO systems," in *2016 IEEE Global Communications Conference (GLOBECOM)*, 2016, pp. 1–6.

[18] Y. Xing and T. S. Rappaport, "Propagation measurements and path loss models for sub-THz in urban microcells," in *2021 IEEE International Conference on Communications (ICC)*, Jun. 2021, pp. 1–5.

[19] M. K. Samimi and T. S. Rappaport, "3-D millimeter-wave statistical channel model for 5G wireless system design," *IEEE Transactions on Microwave Theory and Techniques*, vol. 64, no. 7, pp. 2207–2225, July 2016.

[20] T. S. Rappaport *et al.*, "Millimeter wave mobile communications for 5G cellular: It will work!" *IEEE Access*, vol. 1, pp. 335–349, May 2013.

[21] S. Sun, *et al.*, "MIMO for millimeter-wave wireless communications: beamforming, spatial multiplexing, or both?" *IEEE Communications Magazine*, vol. 52, no. 12, pp. 110–121, 2014.

[22] M. Sanchez-Fernandez, S. Zazo, and R. Valenzuela, "Performance comparison between beamforming and spatial multiplexing for the downlink in wireless cellular systems," *IEEE Transactions on Wireless Communications*, vol. 6, no. 7, pp. 2427–2431, 2007.